THE ASTROPHYSICAL JOURNAL, 464:606–615, 1996 June 20

THE INTENSITY DISTRIBUTION FOR GAMMA-RAY BURSTS OBSERVED WITH BATSE

GEOFFREY N. PENDLETON, ROBERT S. MALLOZZI, WILLIAM S. PACIESAS, MICHAEL S. BRIGGS,
ROBERT D. PREECE, AND TOM M. KOSHUT
Department of Physics, University of Alabama in Huntsville, Huntsville, AL 35899
JOHN M. HORACK, CHARLES A. MEEGAN, AND GERALD J. FISHMAN
NASA/Marshall Space Flight Center, Huntsville, AL 35812
JON HAKKILA
Department of Physics and Astronomy, Mankato State University, Mankato, MN 56002-8400
AND
CRYSSA KOUVELIOTOU
Universities Space Research Association
Received 1995 September 11; accepted 1996 January 9

ABSTRACT

The intensity distributions of gamma-ray bursts observed by BATSE from 1991 April 19 to 1994 September 19 are presented. For this data set, $\langle V/V_{max}\rangle$ is 0.329 ± 0.011, which is 15.5 σ away from the value of 0.5 expected for a homogeneous distribution. Standard cosmological model parameters are obtained by fitting the differentially binned peak flux distribution expressed in units of photons cm^{-2} s^{-1} in the energy range 50–300 keV. The value of z calculated for a peak flux of 1 photon cm^{-2} s^{-1} is 0.8 ± 0.33. The procedures used to produce the peak flux data and C_p/C_{lim} data are presented. The differences between the two representations of burst intensity are emphasized so that researchers can determine which type of data is most appropriate for their studies. The sky sensitivity correction as a function of intensity for the peak flux data is also described.

Subject headings: cosmology: observations — gamma rays: bursts

1. INTRODUCTION

We present here gamma-ray burst peak flux results for BATSE (Fishman et al. 1989) from 1991 April 19 to 1994 September 19, the data set of the BATSE 3B catalog. The peak fluxes are calculated in photons cm^{-2} s^{-1} in the 50–300 keV energy range for the three different BATSE trigger time scales 64, 256, and 1024 ms. These data are essential for measuring the shape of the bursts' intensity distribution.

A question of critical importance to our understanding of gamma-ray bursts is whether the bursts are homogeneous or not. A homogeneous distribution is one where the density of bursts is constant throughout space. The C_p/C_{lim} (Schmidt, Higdon, & Hueter 1988) measure of intensity has been used to determine whether the bursts are distributed homogeneously or inhomogeneously. The technique has the advantage of mitigating the impact of instrument sensitivity on the measurement of the homogeneous distribution. However, once inhomogeneity has been firmly established, as is the case here, then researchers attempting to quantitatively measure the physical nature of the inhomogeneity will want the intensity distribution expressed in physical units. The statistical errors on parameters for models of the burst intensity distribution will not have a precise meaning if the parameter values are determined from the counts data. Burst intensity expressed in counts represents the detector properties applicable to that burst's detection convolved with the burst's true physical intensity.

The peak flux data results from a detailed conversion of the burst's peak flux counts data to physical units. The details of the conversion are described below in sufficient detail to explicitly demonstrate the detector properties and burst detection specifies that differentiate the counts data from the peak flux data.

2. C_p/C_{lim} AS A TEST OF HOMOGENEITY

The calculation of $\langle V/V_{max}\rangle$ for gamma-ray burst intensities is an excellent test of the homogeneity of the gamma-ray burst distribution. For this test, the ratio C_p/C_{lim} is calculated for each burst, where C_p is the peak flux of the burst in counts in the energy range 50–300 keV and C_{lim} is the threshold burst flux in counts for the detector system at the time that C_p is measured. For a standard candle source in Euclidian geometry, one can define the volume V as a sphere, with a radius equal to the distance to a source with intensity C_p, and V_{max} as a sphere, with radius equal to the distance to a source with intensity C_{lim}. Then the ratio V/V_{max} is given by the expression

$$V/V_{max} = (C_p/C_{lim})^{-3/2} . \quad (1)$$

If the distribution of bursts is homogeneous (i.e., if they have constant density throughout space), then the average value of V/V_{max} will be 0.5. This will be true regardless of threshold variations or the shape and extent of broad intrinsic luminosity functions. This is because the shape of the intensity distribution for a homogeneous data set is independent of intensity, that is, it looks the same on any length scale. Therefore, if the data are normalized to the threshold values, then data sets taken with very different detection thresholds will produce statistically equivalent C_p/C_{lim} distributions.

For BATSE, C_{lim} is determined by the background rate and the burst trigger criterion. BATSE triggers when a burst's count rate measured in the 50–300 keV energy range increases by 5.5 σ or more above background in two or more Large Area Detectors (LADs) on one of BATSE's three trigger timescales: 64, 256, or 1024 ms. For a particular burst, then, C_{lim} is 5.5 times the square root of the background rate in the second brightest detector observing that

burst. C_p is determined for the second brightest detector at the peak intensity in counts in the 50–300 keV range of the burst's emission. $C_p/C_{\rm lim}$ then gives the burst's intensity in units of BATSE's trigger threshold.

The largest value of $V/V_{\rm max}$ from each of the three timescales for each burst is used to calculate $\langle V/V_{\rm max}\rangle$ for the entire BATSE 3B catalog data set. As stated above, the $\langle V/V_{\rm max}\rangle$ value is 15.5 σ away from the homogeneous value. The robustness of the $\langle V/V_{\rm max}\rangle$ technique, combined with the strength of the deviation observed by BATSE, ensures the inhomogeneity of the burst population. The $\langle V/V_{\rm max}\rangle$ test can also be used on burst subsets to see if any of them are consistent with homogeneity. However, once deviation from homogeneity has been established for a distribution, precise measurement of the inhomogeneity must employ burst intensities expressed in physical units. Reasons for this requirement are developed below.

3. CALCULATION OF THE PEAK FLUXES

The details of the peak flux calculation are presented below using BATSE trigger 2812 (GRB 940210) as an example. The four channel data from the triggered detectors, in this case LADs 2 and 6, are combined for this analysis. In this case, these two detectors had count rates of 5.5 σ or more at the trigger time and, therefore, were the ones summed on board the spacecraft for the high time resolution burst data. In the interval from -2 to 240 s around the burst trigger time, the data have 64 ms resolution. Outside that interval, they have 1.024 s resolution. Data from separate detectors are also available during the burst interval with 1.024 s resolution. The channels span the energy ranges 25–50, 50–100, 100–300, and $E > 300$ keV, respectively. The background model is produced using a polynomial fit to the data outside the interval where the burst emission occurs. In Figure 1 the count rate in each channel is shown as a thick solid histogram, and the background model is visible as a thin line underneath the burst emission.

Figure 2 shows the 64 ms resolution data for the sum of channels 2 and 3 (50–300 keV) for the summed rates of the burst-selected detectors over an interval that contains the peak flux intervals. The intervals that have the highest source count rates in the 50–300 keV range are selected on the 64, 256, and 1024 ms timescale. The boxed regions in Figure 2 show the peak flux intervals on these three timescales, and, as this example shows, the intersection of these intervals is not required. Once the intervals are selected, the background-subtracted counts per channel are calculated for conversion to physical units.

Figure 3 shows the four-channel count rates for LAD 2 (*diamonds*) and LAD 6 (*crosses*) separately for an interval from GRB 940210. The angle between the detector normal and the burst direction was 7°.5 for LAD 6 and 71° for LAD No. 2. The difference in source viewing angles not only changes the overall count rate between detectors by more than a factor of 2 but changes the ratios between channels as well. The channel 2/1 ratio changes by 50%, the 3/2 ratio by 20%, and the 4/3 ratio by a factor of 2.

To understand the differences between these count rates, it is instructive to examine the detector response matrices (DRMs) for these two detectors evaluated for this burst direction. These functions describe how the instrument converts photon flux into observed counts. The DRMs for BATSE data analysis were generated using a Monte Carlo Electromagnetic Cascade Code coupled to a detailed geometry package. The parameters of the simulation were optimized using exhaustive preflight calibration data. This procedure is described elsewhere (Pendleton et al. 1995a).

Figure 4 shows the detector response for LAD 6 in four separate discriminator channels. The response is shown for each channel in units of counts channel^{-1} detector^{-1} for an incident plane wave of photons with an intensity of 1

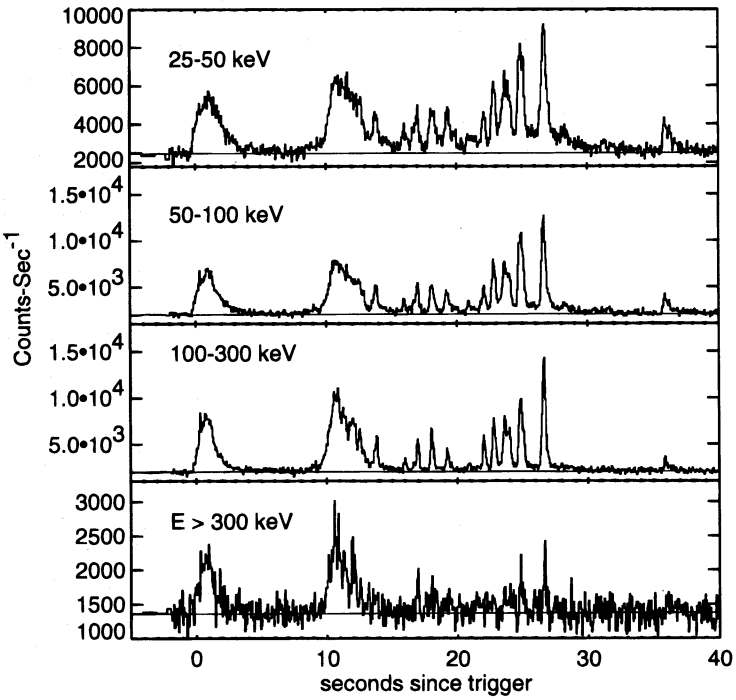

FIG. 1.—Plot showing the data used in the calculation of the background estimate and source counts for the production of the peak flux data. The four channels cover the energy ranges 25–50, 50–100, 100–300, and $E > 300$ keV. The counting rates are represented by the thick histogram, and the background estimate by the thin line.

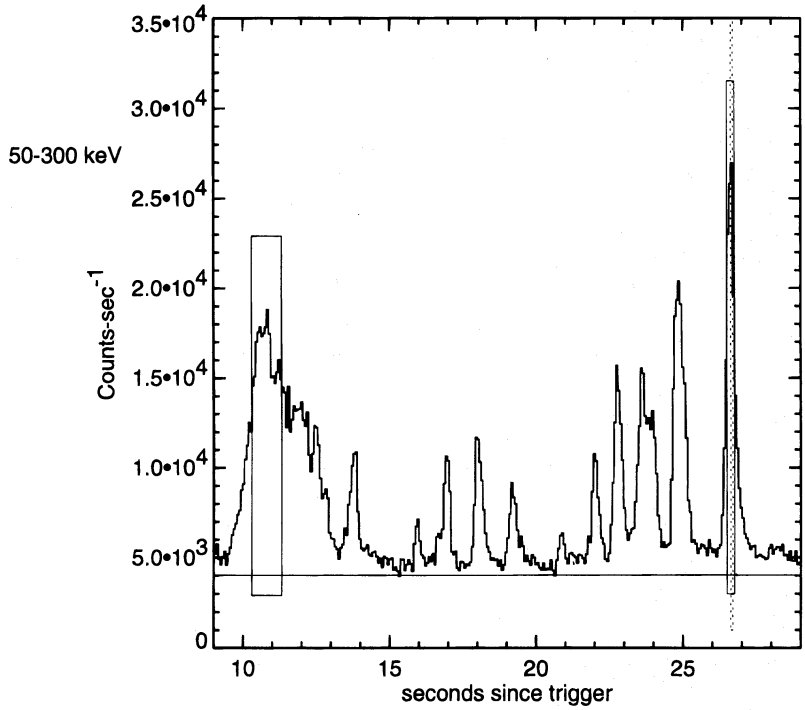

FIG. 2.—Plot of the 64 ms counts data for the 50–300 keV energy range summed over detectors 2 and 6 for the interval containing the peak flux times. The boxes show the intervals selected for the 64, 256, and 1024 ms peak flux intervals. The horizontal line at the bottom is the background estimate.

photon cm^{-2} in the energy range 25–2000 keV. The vertical dashed lines in each plot delineate the energy range of the counts' channel. The plots show that there are significant counts collected in the lower energy channels from higher energy photons (i.e., there is significant cross talk between channels). Figure 5 shows the response function for LAD 2, demonstrating the overall drop in sensitivity of the LADs at larger viewing angles. This is mostly due to the reduced projected area of the detector; however, there are significant energy dependent factors at work here as well. The charged particle detector (CPD) over the front face of the LAD NaI crystal acts as a passive absorber of low-energy photons. As the photon path length through the CPD increases, the low-energy attenuation becomes more significant. Also, partial energy deposition by higher energy photons produces more low-energy counts at large angles of incidence. This can be seen in the LAD 2 25–50 keV response curve, where much of the response is due to photons with energies above 50 keV. The counts between the 25–50 keV and 50–100 keV ranges for LAD 2 are comparable, whereas the 25–50 keV counts are significantly less than the 50–100 keV counts for LAD 6. For LAD 2, the higher energy photon

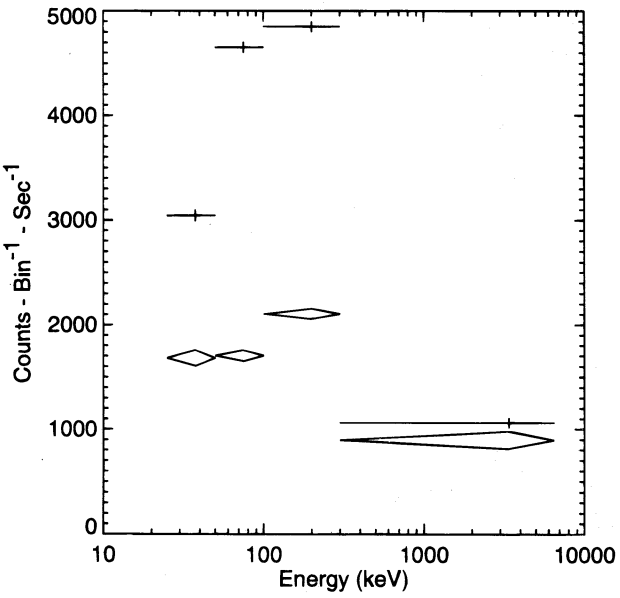

FIG. 3.—The four channel counts spectra for LADs 2 and 6 shown separately for the 9–11 s interval from GRB 940210. This background-subtracted counts data is extracted from the 1024 ms four channel data.

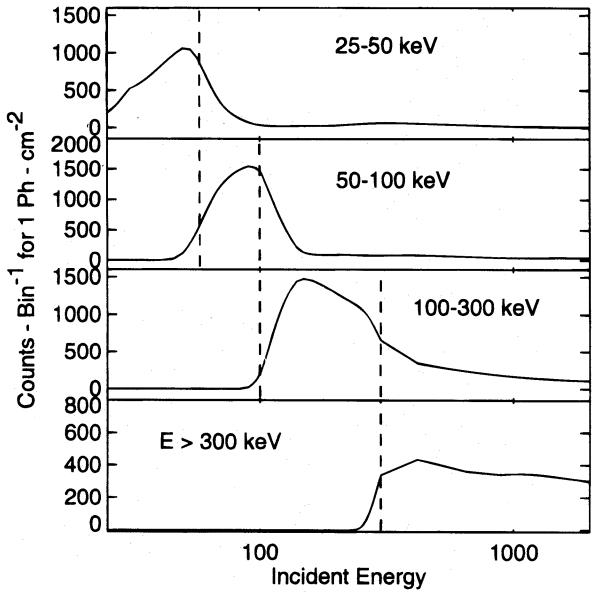

FIG. 4.—Plot of the DRM for LAD 6. The response is displayed in the four LAD discriminator channels as a function of incident photon energy. The vertical dashed lines indicate the energy boundaries of each output channel.

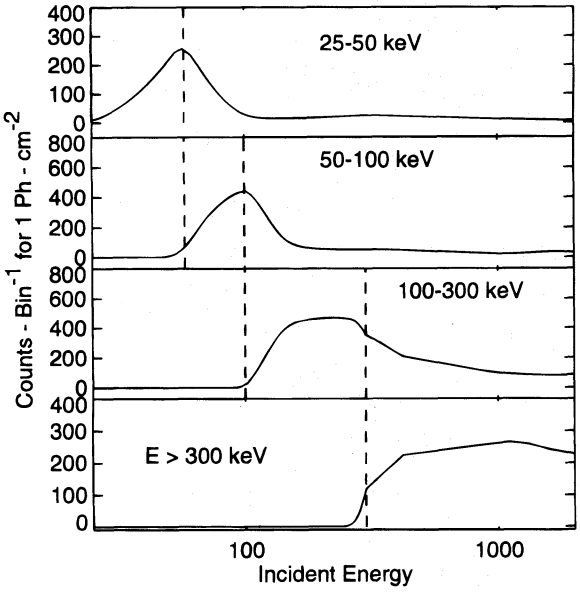

FIG. 5.—Plot of the DRM for LAD 2. The response is displayed in the four LAD discriminator channels as a function of incident photon energy. The vertical dashed lines indicate the energy boundaries of each output channel.

contribution boosts up the 25–50 keV rate relative to the 50–100 keV rate.

At higher energies, the sensitivity of the LAD NaI crystal becomes more volume dependent, and the detector-projected area and path length through the front material is less important. The responses above 300 keV change only marginally for these two different viewing angles. Correspondingly, the differences in the count rates above 300 keV for these two detectors is fairly small compared with the differences at other energies.

Figure 6 shows the DRMs for photon flux scattering off the Earth and into each detector for GRB 940210. The response matrices are calculated for the triggered detectors

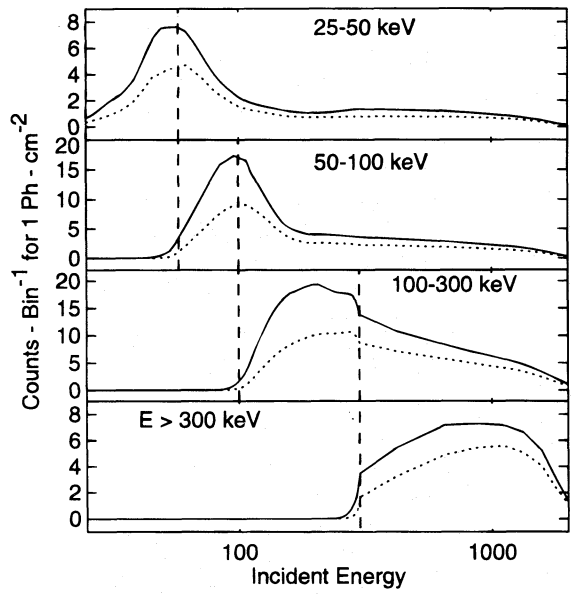

FIG. 6.—Plots of the atmospheric scattering response LADs 2 (*solid line*) and (*dotted line*). The response is displayed in the four LAD discriminator channels as a function of incident photon energy. The vertical dashed lines indicate the energy boundaries of each output channel.

of each burst and used in the spectral deconvolution. In this example, the amplitude of the scattered response is negligible. However, this is not always the case, as will be seen below.

This example shows that the amplitude and hardness ratios for burst fluxes expressed in counts can be highly dependent on the particular conditions of each burst observation. The statistical significances of these quantities expressed in counts measure differences in observing conditions between bursts as well as differences in the physical burst properties.

A direct matrix inversion technique that has been applied successfully to observations of the supernova SN 1987A (Pendleton et al. 1995b) is used here to convert the spectra from counts to photons. For direct inversion, the initial DRM dimensioned 70 × 4 must be cast as a 4 × 4 matrix. Since the bin widths are so wide, some approximation to the spectral shape across each bin is applied. A spectral index of -0.5 is applied across the first three bins, and -1.5 over the highest bin range of 300–6500 keV. This energy range was found to be effective for bursts, and for the Crab Nebula flux measured using four-channel Earth occultation data (Pendleton et al. 1994) The incident energy vectors weighted in this manner are summed across the energy range of each output bin to produce square 4 × 4 DRMs. The DRMs from the separate detectors are summed for use with the summed peak flux data. Then the DRM is inverted and used to produce the photon spectrum using this relation:

$$\mathrm{DRM}^{-1} \times \mathrm{counts} = \mathrm{photons}\ . \qquad (2)$$

At this point, the four-channel photon spectrum expressed as log (photon flux) versus log (energy) is fit with a quadratic polynomial. This quadratic polynomial, being a more accurate representation of the burst spectrum than the initial indices mentioned above, is then used to build a 4 × 4 matrix from the original 70 × 4 matrix a second time. The inversion is performed again, and the final photon fluxes are obtained. These spectra, along with their quadratic fits, are shown in Figure 7. The Peak flux value is calculated by summing the results of channels 2 and 3. Comparisons of the the peak flux analysis results with other detectors' contemporaneous measurements of bursts (Fenimore et al. 1993: Pendleton et al. 1994) indicate that the systematic errors on the peak flux data are about 10%–15%.

In order to illustrate how the detector response characteristics manifest themselves in the $C_p/C_{\rm lim}$ representation of the data, $C_p/C_{\rm lim}$ values for bursts with equivalent peak fluxes are selected. The data in Figure 8 show values of $C_p/C_{\rm lim}$ for the set of 14 bursts with peak fluxes of 1 photon cm^{-2} s^{-1} ± 0.1 on the 1024 ms timescale, effectively picking bursts with fixed intensity in physical units. The crosses in Figure 8 show the $C_p/C_{\rm lim}$ values plotted versus cosine of the angle between the source direction and the second brightest detector, θ. For this set of bursts, θ spans the range from 43° to 67°. These data illustrate the most significant difference between the $C_p/C_{\rm lim}$ data and the physical peak flux; the observed counts for a burst vary to first order as cos (θ). For the BATSE data, this effect is significant; as this example shows, the $C_p/C_{\rm lim}$ values for bursts with the same peak flux can vary by a factor of 3.

Another factor which affects the observed counts in the second brightest BATSE detector is scattering of the burst flux off the Earth's atmosphere into the detector. Figure 9

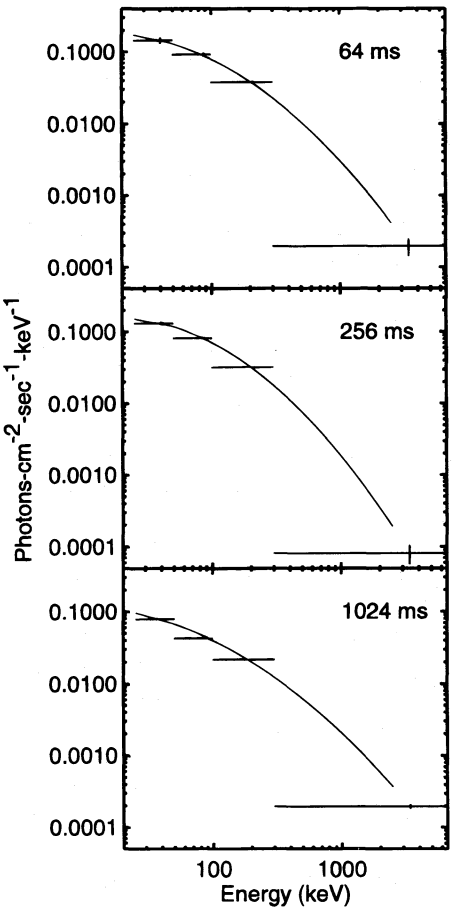

FIG. 7.—Plots of the peak flux data for the three different timescales in the four separate energy bins. A fit to the data is also shown in each plot. The peak flux data is calculated from the sum of the 50–100 keV and 100–300 kev data.

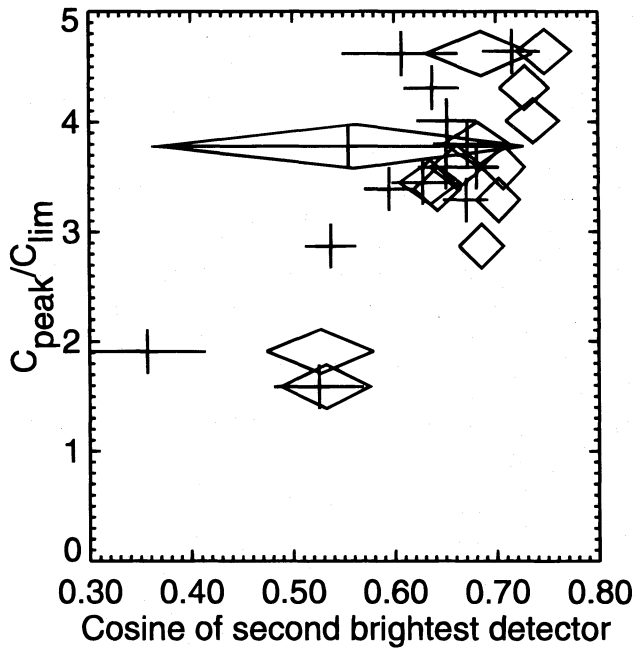

FIG. 8.—Plot showing values of C_p/C_{lim} for an effectively fixed peak flux value vs. simplified representations of the LAD's angular response. The crosses show the C_p/C_{lim} data plotted vs. cosine of the angle between the burst direction and the normal to the second brightest detector, and the diamonds show the data plotted vs. a cosine response crudely corrected for atmospheric scattering.

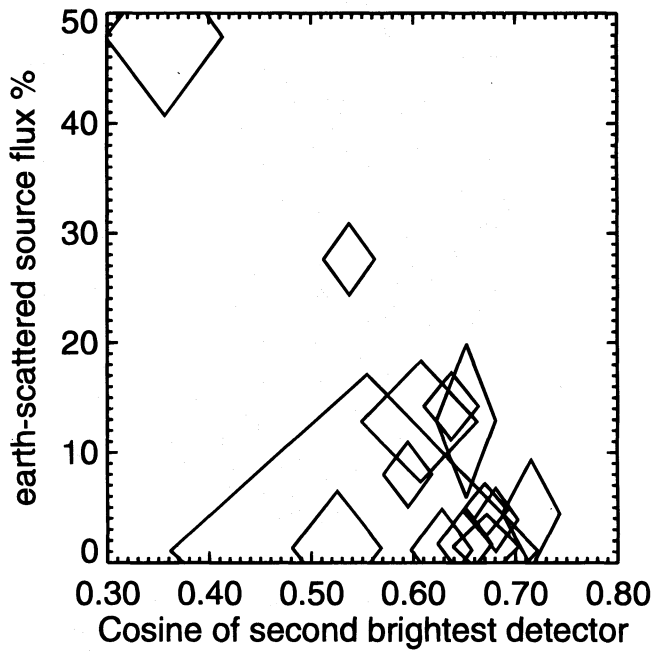

FIG. 9.—Plot showing percentages of Earth scattering flux relative to direct source flux observed in the second brightest detector for a set of bursts with peak fluxes on the 1024 ms timescale of 1 photon cm^{-2} s^{-1}.

shows the ratio of Earth-scattered source counts to direct source counts for the second brightest detector in the 50–300 keV energy range plotted versus cos (θ) for the set of bursts selected in Figure 8. Five of these bursts had Earth-scattered counts in excess of 10% of the direct counts. For these bursts, the Earth scattering produces an excess of counts above what the first order cos (θ) response would predict. One can construct an effective angular response corrected for the atmospheric scattering by assuming that the response is

$$\cos(\theta) \times (\text{direct flux} + \text{scattered flux})/(\text{direct flux}) .$$

The diamonds in Figure 8 show the C_p/C_{lim} data plotted versus this effective angular response. These data exhibit a somewhat stronger linear relationship to the effective viewing angle than the data represented by crosses, indicating that atmospheric scattering has a significant systematic impact on the C_p/C_{lim} values as well. However, even these corrections do not account for all the systematics in the C_p/C_{lim} data. There is also variation in the actual trigger threshold, since the background count rate varies through the Gamma Ray Observatory orbit. Also, the wide variety of spectral forms in bursts (Band et al. 1993; Pendleton et al. 1994) results in very different amounts of high-energy photon flux down scattering into the trigger counts energy range. Since the behavior of the detector angular response is strongly dependent on energy, the spectral diversity affects the trigger counts as well. These instrument properties that affect the C_p/C_{lim} data are corrected in the peak flux data.

4. INTENSITY DISTRIBUTIONS FOR GAMMA-RAY BURSTS

Figures 10*a*–10*c* show the integral log N–log P distributions on the three different timescales: 64, 265, and 1024 ms, respectively. (Fig. 10*a* also shows the overwrite bursts that will be discussed below.) In these units, it can be seen that

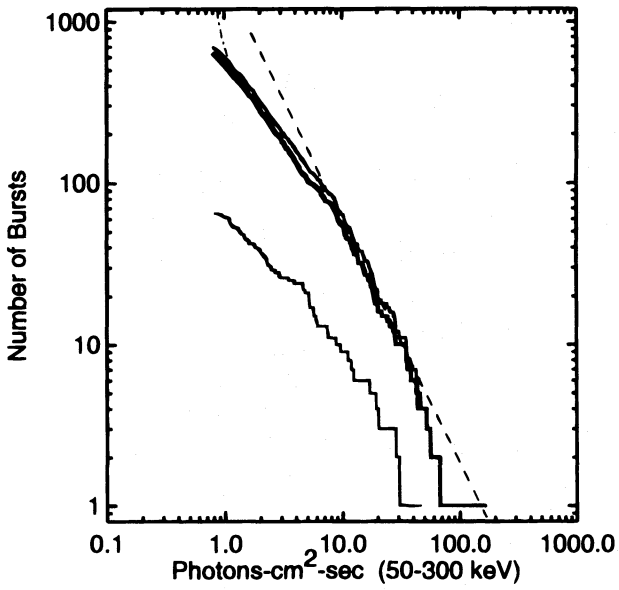

FIG. 10*a*

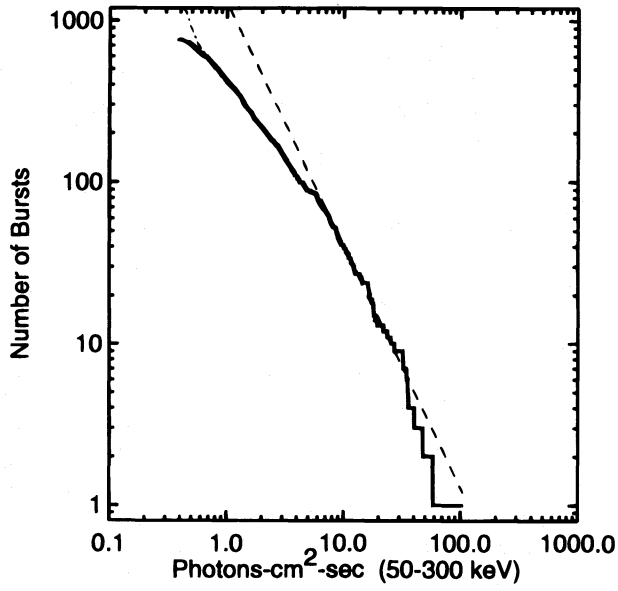

FIG. 10*b*

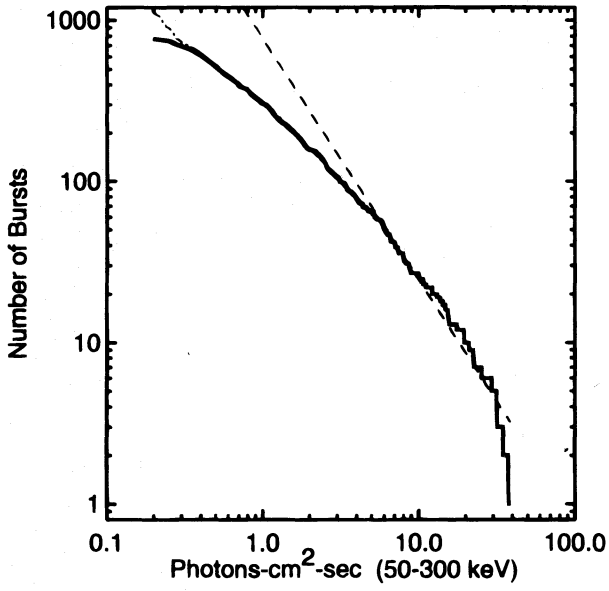

FIG. 10*c*

FIG. 10.—(*a–c*) Plots showing integral peak flux distributions, with a $-3/2$ power-law tangent to the bright end of the distributions shown as a dotted line. (*a*) The thick histogram shows a 64 ms peak flux rate in the 50–300 keV range with overwrite bursts removed. The thinner histogram above this one is the total distribution. The lowest thinner histogram is the peak flux distribution for the overwrite bursts. The dot-dashed line at the end of the thick histogram represents the outer envelope for the distribution correction due to the decrease in sensitivity of the instrument as a function of intensity. (*b*, *c*) Peak flux distributions for the nonoverwrite bursts and the sensitivity correction for the 256 and 1024 ms timescales, respectively.

the longer timescales have lower threshold rates than the short timescales. The threshold rate for an interval in counts s^{-1} is 5.5 times the square root of the number of counts (σ) in the interval divided by the interval duration. For a fixed background rate, the number of background counts in the 1024 ms interval is 16 times that in a 64 ms interval, so $\sigma_{1024\ \mathrm{ms}}$ is 4 times $\sigma_{64\ \mathrm{ms}}$. However, 1024 ms is 16 times 64 ms, so the threshold rate [σ/(interval duration)] for 1024 ms is 4 times smaller than for 64 ms.

Hence, the longer timescales can allow for more precise calculations of the rates due to better counting statistics for bursts with flux at the peak rate for 1 s or more; the 1024 ms timescale is 4 times as sensitive as the 64 ms timescale for bursts with longer peak rate emission. For bursts with peak flux rate durations of less than 1024 ms, the relative sensitivity between trigger timescales becomes a general function of the flux versus the time profile. For this reason, the peak flux data should not be mixed between timescales without explicitly calculating the effect of the flux versus the time profiles of the bursts involved on the peak flux values and thresholds.

In order to ensure the accuracy of peak flux data used to characterize the intensity distribution, it is necessary to investigate the changes in the instrument sensitivity, or sky exposure, near threshold. The sky exposure for BATSE is a function of burst peak intensity and changes significantly

near threshold. The primary contributor to this change is the variation in incident angle to the second brightest detector with position on the sky (Brock et al. 1992). As can be seen in Figure 8, the count rate in the second brightest detector can vary greatly for bursts with the same intensity. Regions of the sky that see the second brightest detector at large angles become insensitive to weaker bursts.

The temporal variation in the background rates due to orbital variations also affects the sensitivity near threshold. The thin histogram in Figure 11 (to be described in detail below) shows the distribution of $C_{\rm lim}$ values for the 64 ms timescale spanning a range for 50 to 85 counts. This is the variation in the trigger threshold that is 5.5 times the square root of the background counts in 64 ms in the 50–300 keV energy range at the burst trigger times. The histogram shows that the instrument sensitivity to bursts with 64 ms peak counts of 50 is considerably less than for bursts with 64 ms peak counts of 85.

These two contributors to the variation in exposure near threshold are incorporated into the sky exposure calculation. A correction for the exposure as a function of burst intensity is shown as a thin line at the low-intensity end of the Figure 6 plots, This correction shows where the exposure starts to affect the shape of the burst intensity distribution. However, the correction, as it stands, underestimates BATSE's sensitivity near threshold and, consequently, produces an overcorrection to the intensity distribution.

What is missing from the current calculation of the sky exposure is the enhancement of the source counts measured by the second brightest detector, due to atmospheric scattering (Pendleton et al. 1992). Figure 9 shows that atmospheric scattering increases the source flux in the second brightest detector for a significant number of bursts, particularly those that have larger burst viewing angles. Including this correction will increase the calculated sensitivity to bursts near threshold and, hence, remove the effect of the intensity distribution overcorrection near threshold. The intensity correction currently should be used to limit the intensity range of the burst data set used for calculating burst intensity distribution model parameters. The sensitivity corrections in Figures 10*a*–10*c* show that the change in BATSE's sensitivity with intensity becomes insignificant at about twice the photon flux threshold. Since the break in the log N–log P slope from a 3/2 power law obviously occurs at much higher intensities, changes in the sky sensitivity cannot be invoked to explain it.

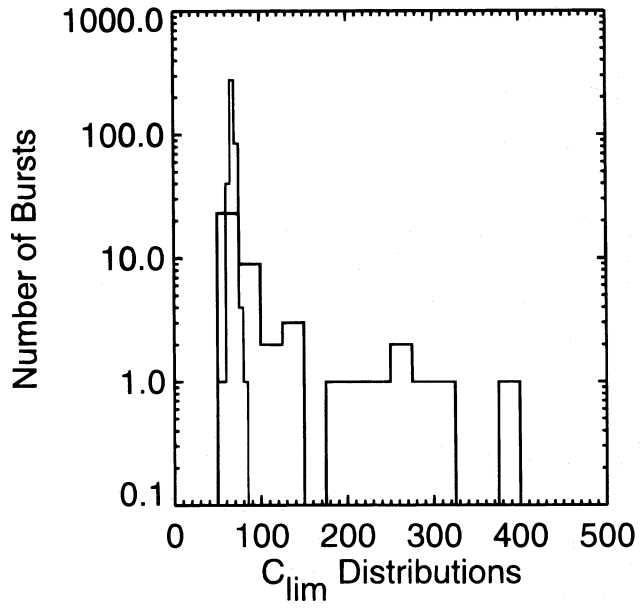

FIG. 11.—Plot showing the distribution of thresholds in counts for the 64 ms timescale. The thin histogram is the threshold distribution for the nonoverwrite bursts, and the thick histogram is the overwrite burst threshold distribution.

Figure 10*a* also shows the log N–log P distribution for the overwrite bursts. When the instrument is triggered, no other triggers are possible during the burst accumulation time (typically 240 s). Then, during the burst readout time (typically 90 minutes), the trigger threshold is increased to the peak count rate of the accumulated burst for the 64 ms threshold. This is calculated from a 1 s peak counts accumulation converted to a 64 ms rate. The 256 and 1024 ms triggers are disabled during readout. This is done so that the brightest burst at the time is recorded. If, during trigger readout, a burst occurs that is brighter than the burst being read out on the 64 ms timescale, then the readout in progress is aborted and a new burst accumulation begins. This procedure increases BATSE's sensitivity to bright, potentially interesting bursts and produces a data subset called overwrite bursts.

The log N–log P distribution for the overwrite bursts has a noticeably smaller fraction of weak bursts than the general population. This is expected, since bursts have to be brighter than an already triggered event to become overwrite bursts. However, the $\langle V/V_{\rm max}\rangle$ value for the overwrites is 0.42 ± 0.047, which is larger than the general population value. From spatial considerations alone, we would expect the flatter overwrite distribution of Figure 6*a*, to have a smaller, $\langle V/V_{\rm max}\rangle$ value than the general population since there are fewer weak overwrite bursts. Indeed, if we calculate $P_p/P_{\rm lim}$ (i.e., divide each peak flux value by the smallest peak flux value in the distribution) for the overwrite bursts and calculate the corresponding $\langle V_p/V_{p,\,\rm max}\rangle$ value, we get 0.16 ± 0.025. This apparent discrepancy is understood when one takes into account the highly variable threshold that affects the overwrite bursts.

Figure 11 shows the 64 ms trigger count threshold distributions for the general burst population (*thin histogram*) and for the overwrite bursts (*thick histogram*). It is the broad distribution of $C_{\rm lim}$ values of the overwrite bursts that cause the $\langle V/V_{\rm max}\rangle$ value to be relatively high. In this case, the $\langle V/V_{\rm max}\rangle$ value reflects the operating characteristics of the instrument, not the physical structure of the underlying burst distribution. Measurement of the burst intensity distribution here requires conversion to physical units and careful calculation of the instruments sensitivity as a function of burst intensity.

Now that the specific causes of the discrepancies between the peak flux and the $C_p/C_{\rm lim}$ values have been reviewed, it is intructive to compare the burst intensity distributions in these two representations and see how they differ.

Figure 12 (panel 12A) shows the integral peak flux distribution (*thick line*) and the integral $C_p/C_{\rm lim}$ distribution (*thin line*) for the set of bursts that have both $C_p/C_{\rm lim}$ and peak flux values calculated on the 1024 ms timescale. The peak fluxes are given in units of flux above the 1024 ms peak flux threshold. The K-S test comparing these two data sets shows them to be different at the 2.2×10^{-11} probability level. This is largely due to the differences in the distributions near threshold. The downturn in the slope of the peak

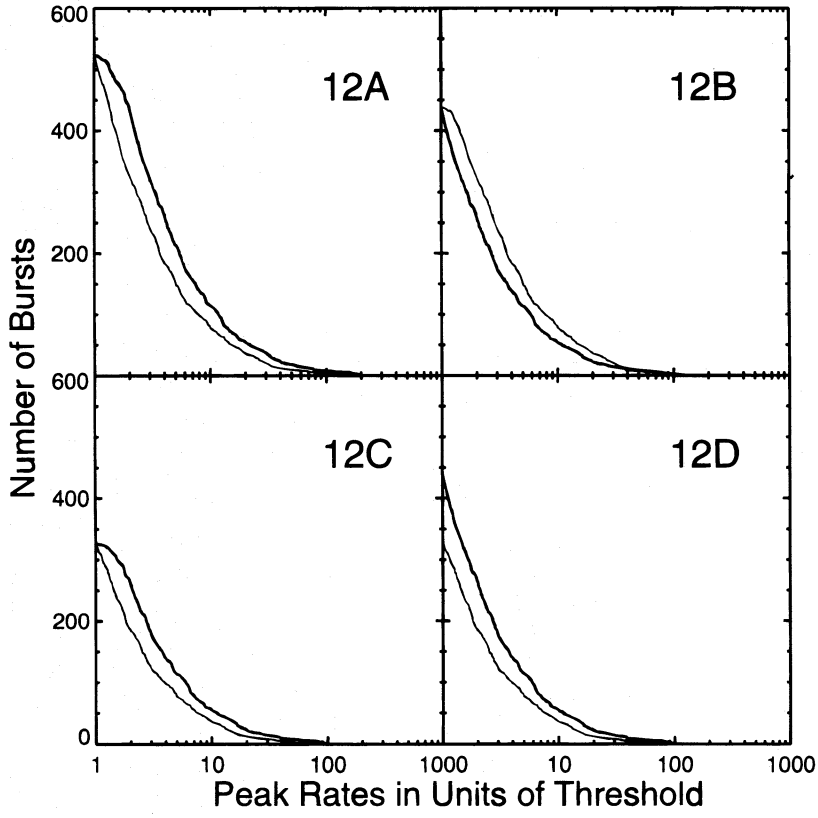

FIG. 12.—Plots showing comparisons between peak flux and C_p/C_{lim} integral distributions. 12A: distributions for an identical set of bursts above threshold. 12B: distributions selected for bursts with peak fluxes twice the photon flux threshold. 12C: distributions selected for bursts with C_p/C_{lim} values greater than or equal to 2. 12D: the C_p/C_{lim} distribution selected with the 12C criterion and the peak flux distribution selected with the 12B criterion.

flux data at threshold shows where the instrument sensitivity starts to significantly affect the distribution. Without detailed exposure correction, the shape of the log N–log P curve below about twice the photon flux is unknown. However, a researcher fitting a physical model to the peak flux distribution can use the data in the region of uniform exposure and produce quantitative results with meaningful parameter errors.

The C_p/C_{lim} distribution is insensitive to instrument sensitivity variations near threshold since it is designed to test the assumption of homogeneity, a case where the shape of the log N–log P curve is not a function of intrinsic burst luminosity. It does not show the decrease in exposure near threshold that is apparent in the peak flux distribution. Bursts selected from a narrow range of C_p/C_{lim} at threshold are actually distributed over a broader range, from the peak flux threshold to slightly above the upper end of the peak flux range where exposure corrections are important. The intensity distribution near threshold expressed in C_p/C_{lim} does not map monotonically onto the intensity distribution expressed in physical units. This distortion of the C_p/C_{lim} intensity distribution compromises the accuracy of any intensity distribution parameter estimates derived from the C_p/C_{lim} data set.

One can check to see if selecting bursts that are above the region where the sky sensitivity corrections are important produces similar peak flux and C_p/C_{lim} distributions. Figure 12 (panel 12B) shows the distributions for the subset of burst where the peak fluxes are twice the peak flux threshold. Here the peak fluxes are divided by twice the peak threshold. These data sets are different at the 7.1×10^{-5} probability level. The C_p/C_{lim} curve shows a gradual drop-off near the threshold, demonstrating that the photon threshold does not map precisely onto the C_p/C_{lim} threshold even above the range where instrument sensitivity significantly affects the exposure.

One can try selecting bursts where $C_p/C_{lim} \geq 2.0$ to escape threshold effects. Figure 12 (panel 12C) shows the distributions obtained with this selection criterion. Here the C_p/C_{lim} values are divided by 2, and the peak flux values are divided by the peak flux threshold. This simply moves the threshold effects present in Figure 12 (panel 12A) up to a higher flux level. These distributions show inconsistency at the 2.3×10^{-9} probability level.

However, one can find C_p/C_{lim} and peak flux distributions that are similar. If we take the C_p/C_{lim} distributions for those bursts with $C_p/C_{lim} \geq 2.0$ and the peak flux distribution for bursts where the flux is greater than or equal to twice the photon flux threshold, then the distributions are consistent at the 0.77 probability level. Figure 12 (panel 12D) shows the distributions divided by their respective selection thresholds. These are no longer identical data sets. The C_p/C_{lim} distribution has fewer bursts in it because, as is seen in Figure 12 (panel 12A), many bursts with peak fluxes greater than twice the photon threshold have $C_p/C_{lim} < 2$.

Based on these comparisons, one can say that the C_p/C_{lim} distribution is qualitatively similar to the log N–log P distribution, well above the instrument threshold for representing structure that does not change significantly over a range of a factor of 3. However, it is important to use the photon peak flux distributions to estimate the impact of threshold effects on the distribution. Clearly, quantitative error analysis comparing the C_p/C_{lim} distribution to physical models of the burst intensity distribution is not advanta-

geous, since known instrumental behavior affects this data in addition to the statistical uncertainties.

5. MEASURING THE INHOMOGENEITY OF THE log N–log P DISTRIBUTION

The $\langle V/V_{max} \rangle$ value of this data set shows a clear deviation from homogeneity. Furthermore, previous analysis of a combined *PVO*-BATSE data set (Fenimore et al. 1993) shows the existence of a change in slope versus peak flux in the log N–log P distribution for gamma ray bursts.The distribution is consistent with homogeneity in the *PVO* data set and for the brightest BATSE bursts. Here the current data set is analyzed to determine the strength of the break in the intensity distribution's slope using the BATSE data alone.

The log N–log P data is coarsely binned into statistically independent peak flux bins covering the range from the brightest burst to just where the sensitivity corrections become significant. The data are then fitted with a power law using a χ^2 test to determine the goodness of the fit. Single power law χ^2 fits to differentially binned flux data are still marginally consistent. The 256 ms data is consistent at the 5% level with an integral intensity distribution slope of -0.93. Extrapolation of the current data set indicates that increasing it by a factor of 2 will drop this consistency to 0.1%. At that point, it may be possible to study the structure of the log N–log P distribution to see if the change in slope occurs quickly over a restricted range or gradually over an extended range, as is predicted by conventional cosmological models.

Most of the BATSE log N–log P data populates the range where the slope of the distribution differs significantly from $-3/2$ and the data is inconsistent with the $-3/2$ power law on all three trigger timescales. The extrapolation of a $-3/2$ power law normalized to the 256 ms distribution above a peak flux of 10.15 photons cm^{-2} s^{-1} overestimates the flux in the range 0.77–0.98 photons cm^{-2} s^{-1} by a factor of 6.6. This is above the flux level where the sensitivity corrections are important and is significant at the 58 σ level.

In order for this deficit to be due to some kind of selection effect, BATSE would have to be missing 85% of the bursts in the 0.77–0.98 photons cm^{-2} s^{-1} peak flux range. This kind of selection effect would produce significant differences between the low-intensity and high-intensity burst population properties. In Figure 12, comparisons are made for the durations and spectral indices in the 50–300 keV range between a set of dim bursts with fluxes in the 0.77–0.92 photons cm^{-2} s^{-1} range and a set of bright bursts with fluxes greater than 6.36 photons cm^{-2} s^{-1} on the 256 ms timescale. Figure 13*a* shows the bright burst duration distribution (*solid histogram*) with the dimmer burst distribution (*dotted histogram*). These distributions cover the same range and show no evidence for differences that would account for a 85% deficit. Figure 13*b* shows the bright (*solid histogram*) and dim (*dotted histogram*) peak flux spectral index distributions for the 256 ms timescale. There is a noticeable softening of the dim bursts relative to the bright bursts as has been reported elsewhere (Norris et al. 1995), but the range of the distributions is still the same and there is a 66% overlap between them. There is no evidence in the burst population for selection effects causing the intensity deficit based on differences in these other burst observables; hence, it should be considered a physical property of the gamma-ray burst intensity distribution.

6. FITS OF CONVENTIONAL COSMOLOGICAL MODELS TO THE DATA

Fits of standard cosmological models to the log N–log P distribution have been made with the assumption of a standard candle burst luminosity. Since a proper treatment of Galactic models includes fits to both the bursts' log N–log P distribution and their angular distribution, these models will not be discussed here. The rate density of bursts per comoving volume is assumed to be constant as well. The procedure used here is similar to that described in Fenimore et al. (1993). The cosmological parameters used here are $H_0 = 75$ km s^{-1} Mpc^{-1} and $q_0 = 0.5$. The fit is shown in Figure 14 as the solid histogram superimposed over the

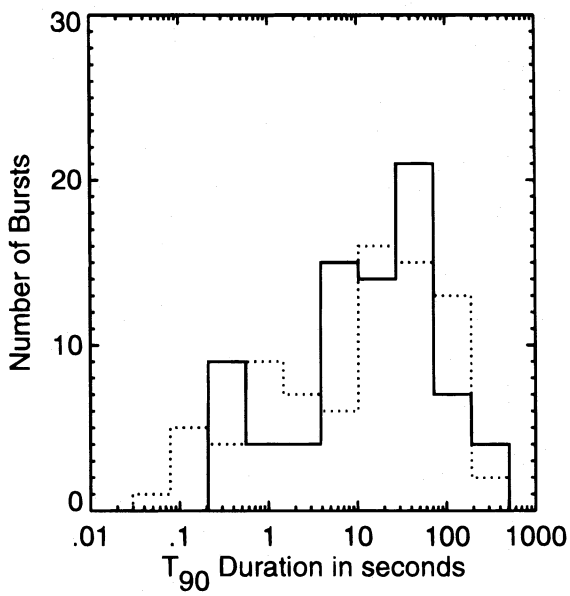

FIG. 13*a*

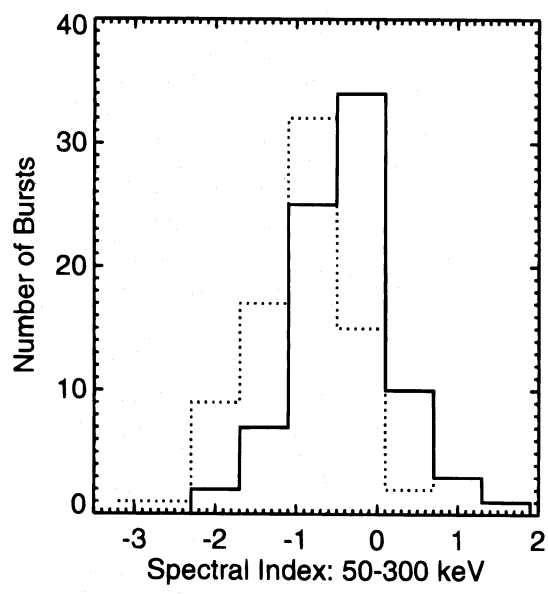

FIG. 13*b*

FIG. 13.—(*a*, *b*) Plots showing distributions of burst observables for two sets of bursts selected by intensity on the 256 ms timescale. The solid histograms are for bursts with peak fluxes in the $P > 6.36$ photons cm^{-2} s^{-1} range, and the dotted histograms are for bursts in the $0.77 < P < 0.92$ photons cm^{-2} s^{-1} range. (*a*) Duration distributions, and (*b*) Spectral index distributions in the 50–300 keV range.

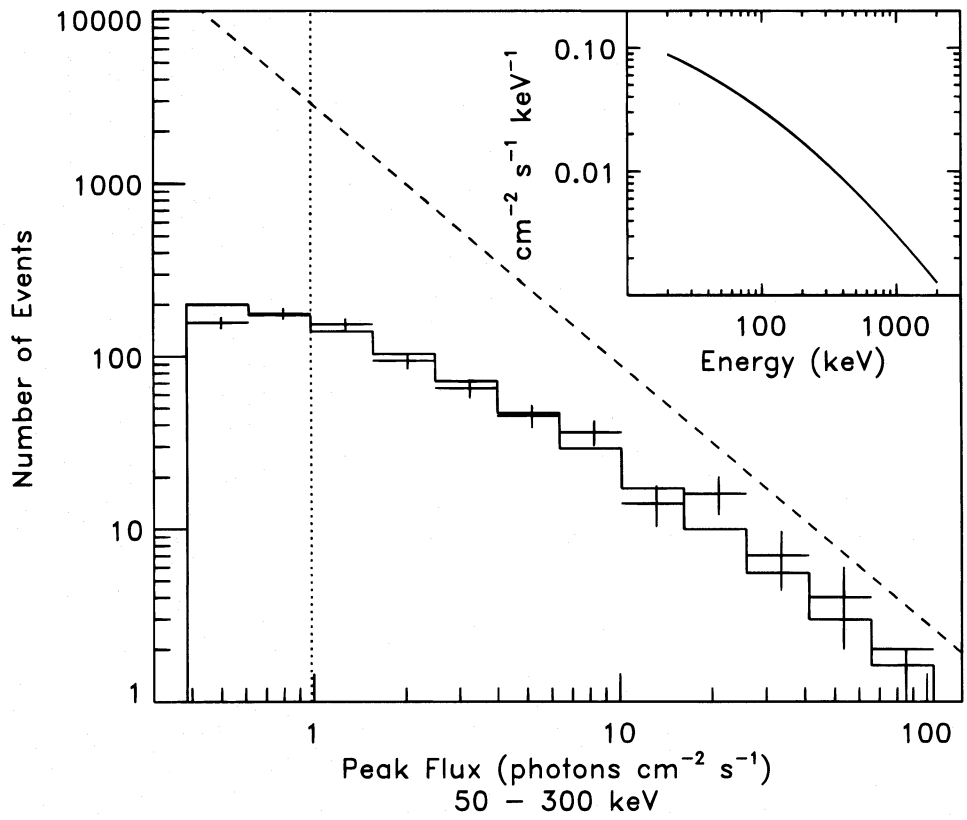

FIG. 14.—Fit of a conventional cosmological model to the differential log N–log P data on the 256 ms timescale. The crosses represent the data, and the solid histogram represents the fit. The data are fitted only above the vertical dotted line to exclude the intensity region where exposure corrections are significant. The dashed line is the $-3/2$ power law for a homogeneous Euclidean distribution. The spectrum inset in the upper right-hand corner of the figure was used in the cosmological model as the representative burst spectrum. The fit has a χ^2 of 8.11 for 8 degrees of freedom.

data represented by crosses. The spectral model used is the quadratic fit of $\log_{10}(P)$–$\log_{10}(E)$ described earlier for a typical bright burst shown in the upper right-hand corner of the plot. The effect of variation in the burst spectrum on the fitted parameters is discussed elsewhere (Mallozzi et al. 1995). The 256 ms data are binned into 12 logarithmically spaced bins, and the 10 bins above the threshold region are used for the model fits. The value of z calculated for the flux 1 photon cm^{-2} s^{-1} is 0.08 ± 0.33, consistent with the BATSE/*PVO* calculation. Application of the moments technique (Horack, Emslie, & Hartmann 1995) to this data using an E^{-2} spectral form yields results in agreement with threshold values for z.

These data lend themselves naturally to a simple cosmological explanation. However, the morphology of burst behavior is quite complex, and all aspects of burst behavior, including spectral softening and time dilation (Mallozzi et al. 1995; Norris et al. 1995), must be shown to be consistent with a single cosmological scenario before the cosmological origin of gamma-ray bursts can be conclusively proved. The effect of hardness intensity correlations based on the physical definitions of these quantities, as well as correlations between intrinsic burst luminosity and other burst observables, should be explored as well. The cosmological scenarios predict a functional relationship between the burst intensity and the other burst observables: emission peak durations and their spectra. With a large enough data set, this functional relationship should be apparent in the differential distribution of these burst observables, not only as a shift between bright and dim bursts but as a trend in the differentially binned data that exhibits the predicted cosmological form. If the burst data set with 2000–3000 entries exhibits trends that are not consistent with cosmological predictions, then the cosmological interpretation for the observed intensity distribution will no longer be a much simpler, more natural explanation for the burst observations than the extended Galactic halo. In any event, these studies should be performed in physical units to minimize the distortions introduced by instrument systematics.

REFERENCES

Band, D., et al. 1993, ApJ, 413, 281
Brock, M. N., Meegan, C. A., Roberts, F. E., Fishman, G. J., Wilson, R. B., Paciesas, W. S., & Pendleton, G. N. 1992, in Proc. First Gamma-Ray Burst Workshop, ed. W. Paciesas & G. Fishman (New York: AIP), 399
Fenimore, E. E., et al. 1993, Nature, 336, 40
Fishman, G. J., et al. 1989, in Proc. GRO Science Workshop, Vol. 2, ed. N. Johnson (Washington, DC: NRL), 39
Horack, J. M., Emslie, A. G., & Hartmann, D. H. 1995, ApJ, 447, 474
Mallozzi, R. S., Paciesas, W. S., Pendleton, G. N., Briggs, M. S., Preece, R. D., Meegam, C. A., & Fishman, G. J. 1995, ApJ, 454, 597
Norris, J. P., Bonnell, J. T., Nemiroff, R. J., Scargle, J. D., Kouveliotou, C., Paciesas, W. S., Meegan, C. A., & Fishman, G. J. 1995, ApJ, 439, 542
Pendleton, G. N., et al. 1994, ApJ, 431, 416
Pendleton G. N., et al. 1995a, Nucl. Instrum. Methods Phys. Res. A, 364, 567
Pendleton, G. N., Paciesas, W. S., Fishman, G. J., Meegan, C. A., & Wilson, R. B. 1995b, ApJ, 439, 963
Pendleton, G. N., et al. 1992, in Proc. Compton Observatory Science Workshop, ed. R. Shrader, N. Gehrels, & B. Dennis (NASA CP 3137), 47
Schmidt, M., Higdon, J. C., & Hueter, G. 1988, ApJ, 329, L85